Journal of Innovative Materials in Extreme Conditions
2026
Volume 7
Issue 1

FIRST-PRINCIPLES AND EXPERIMENTAL INVESTIGATION OF THE THERMOELECTRIC PROPERTIES OF $(Ba_{0.33}Ca_{0.33}Sr_{0.33})(Ti_{0.33}Zr_{0.33}M_{0.33})O_3$, (M = Nb, Sn, Hf) HIGH ENTROPY PEROVSKITE OXIDES

Imrongnaro LONGKUMER[1]***, Subrahmanyam BANDARU***[1]***, Hakan ÜNSAL***[1]***, Asif ALI***[1]***,***
Nikola KANAS[2]***, Vladimir V. SRDIĆ***[3]***, Ondrej HANZEL***[1]***, Magdaléna PRECNEROVÁ***[4]***,***
Peter TATARKO[1,*]

[1] *Institute of Inorganic Chemistry, Slovak Academy of Sciences Bratislava, Slovakia*
[2] *TEGMATICA Ltd., Kikinda, Serbia*
[3] *Department of Materials Engineering, Faculty of Technology Novi Sad, University of Novi Sad, Novi Sad, Serbia*
[4]*Centre for Advanced Materials Application, Slovak Academy of Sciences Bratislava, Slovakia*
[*] *Corresponding author:* ***Peter Tatarko*** *(peter.tatarko@savba.sk)*

Abstract: *High-entropy perovskite oxides (HEPOs) have emerged as promising thermoelectric materials owing to their exceptional structural stability and intrinsically low lattice thermal conductivity arising from severe lattice distortion and configurational disorder. In this work, the structural, electronic, and thermoelectric properties of three HEPOs,* $(Ba_{0.33}Ca_{0.33}Sr_{0.33})(Ti_{0.33}Zr_{0.33}M_{0.33})O_3$ *(M = Nb, Sn, and Hf), were investigated using a combination of first-principles density functional theory calculations and experimental characterisation. The calculations revealed that Nb substitution induces metallic behaviour, resulting in enhanced electrical conductivity and power factor, whereas the Sn- and Hf-containing compositions retained semiconducting characteristics. The relatively weak contribution of Sn-derived states near the Fermi level accounted for its inferior electronic transport. Experimental synthesis and characterisation confirmed the theoretical predictions. Although the Nb-containing composition exhibited superior electrical transport, the Hf-containing HEPO achieved the highest thermoelectric figure of merit (ZT) owing to its significantly reduced thermal conductivity. These findings demonstrate that B-site compositional engineering effectively tailors the electronic structure and thermoelectric performance of high-entropy perovskite oxides, providing valuable design guidelines for next-generation high-temperature oxide thermoelectric materials.*

Keywords: *high entropy perovskite oxides, thermoelectrics, density functional theory, Boltzmann transport*

1. Introduction

The increasing global demand for energy and the negative impact of fossil fuels on environmental have driven the development of sustainable energy technologies. Among the various renewable energy solutions, thermoelectric (TE) technology offers the unique capability to directly convert waste heat into electrical energy. Thermoelectric materials possess several inherent advantages, including silent operation, high reliability, scalability, and the absence of moving parts. The performance of a TE material is commonly evaluated by the dimensionless figure of merit $ZT(= S^2\sigma T/\kappa$, where S is the Seebeck coefficient, σ is the electrical conductivity, κ is the thermal conductivity, and T is the absolute operating temperature. Consequently, an ideal TE material should exhibit a high power factor ($S^2\sigma$) together with low thermal conductivity (κ), thereby maximising the ZT value.

Conventional TE materials, such as Bi_2Te_3, PbTe, and silicon-germanium alloys, exhibit excellent TE performance [1-5]. However, their widespread application is restricted by the scarcity of constituent elements, toxicity, and relatively high production costs. In recent years, oxide-based TE materials have attracted considerable attention as promising candidates for high-temperature power generation owing to their excellent chemical stability, oxidation resistance, and environmental compatibility. Among these, perovskite oxides have emerged as particularly attractive materials because of their exceptional structural flexibility and the possibility of tailoring both electronic and phonon transport through compositional engineering.

In recent years, entropy engineering through multi-cation substitution has been recognised as an effective strategy for enhancing TE performance [6]. In perovskite oxides with the general formula ABO_3, the incorporation of multiple elements at crystallographic A and B sites introduces substantial lattice distortion, mass fluctuation, and chemical disorder, which can efficiently scatter thermal phonons and reduce lattice thermal conductivity. Simultaneously, careful selection of cations enables modification of the electronic structure, allowing optimisation of carrier concentration and transport properties. The combination of high configurational entropy and compositional flexibility makes high-entropy perovskite oxides (HEPOs) an attractive platform for simultaneously tailoring electrical and thermal transport characteristics.

In the present work, three HEPO compositions, $(Ba_{0.33}Ca_{0.33}Sr_{0.33})(Ti_{0.33}Zr_{0.33}M_{0.33})O_3$ (M = Nb, Sn, Hf) were investigated. Ba, Ca, and Sr were fixed at the A-site, while Ti and Zr were selected as the primary B-site cations because of their stable oxidation states and their suitability for tuning the electronic transport properties. Nb, Sn, and Hf were introduced as the third B-site cations to further modify both the electronic and thermal transport behaviour. Specifically, Nb^{5+} acts as an electron donor, increasing the carrier concentration and thereby improving electrical conductivity [7]. Hf^{4+}, owing to its relatively high atomic mass, enhances phonon scattering through increased mass fluctuations [8]. In contrast, Sn^{4+} modifies the electronic band structure and induces local lattice distortions, both of which can significantly influence TE performance [9].

To establish a comprehensive structure–property relationship, first-principles density functional theory (DFT) calculations were performed to investigate the structural stability and electronic properties of the investigated compounds. Temperature-dependent transport coefficients, including the Seebeck coefficient, electrical conductivity, and power factor, were subsequently evaluated using the Boltzmann transport formalism implemented in the BoltzTraP code. Experimentally, the materials were synthesised by a conventional solid-state route and characterised using X-ray diffraction (XRD), scanning electron microscopy (SEM), and X-ray photoelectron spectroscopy (XPS) to confirm phase formation, microstructure, and chemical composition. Thermoelectric properties of the materials were subsequently measured over a wide temperature range and compared with the theoretical predictions.

The aim of the present study was to elucidate the influence of B-site compositional complexity on the electronic structure and thermoelectric performance of entropy-stabilised perovskite oxides. By combining first-principle calculations with comprehensive experimental characterisation and transport measurements, this work provides valuable insights into the design principles governing next-generation oxide thermoelectric materials for high-temperature energy harvesting applications.

2. Computational study of structural, electronic and thermoelectric properties

2.1. Computational methods

First principles calculations were performed using the DFT package VASP (Vienna Ab initio Simulation Package), employing the projector-augmented-wave (PAW) method and the Perdew-Burke-Ernzerhof (PBE) exchange-correlation functional [10-14]. A plane-wave cutoff energy of 550 eV was used throughout all calculations. To model the chemical disorder in HEPOs, 2 × 2 × 3 supercells containing 60 atoms were constructed using the special quasi-random structure (SQS) approach for the study of the electronic structure and transport properties of all compounds [15, 16]. Self-consistent electronic structure calculations were carried out using a Monkhorst-Pack *k*-point mesh of 6 × 6 × 4, corresponding to 72 *k*-points in the irreducible Brillouin zone of the supercell. Electronic transport properties were subsequently evaluated using the BoltzTraP code within the constant relaxation time approximation [17]. To ensure convergence of the calculated transport coefficients, the band energies were interpolated in a non-self-consistent manner onto a denser 18 × 18 × 12 *k*-point mesh, corresponding to approximately 2000 *k*-points in the irreducible Brillouin zone. The electronic self-consistency criterion was to 10^{-5} eV, while the atomic structures were relaxed until the residual forces on each atom were below 10^{-6} eV/Å.

2.2. Crystal structure and electronic structure of $(Ba_{0.33}Ca_{0.33}Sr_{0.33})(Ti_{0.33}Zr_{0.33}M_{0.33})O_3$

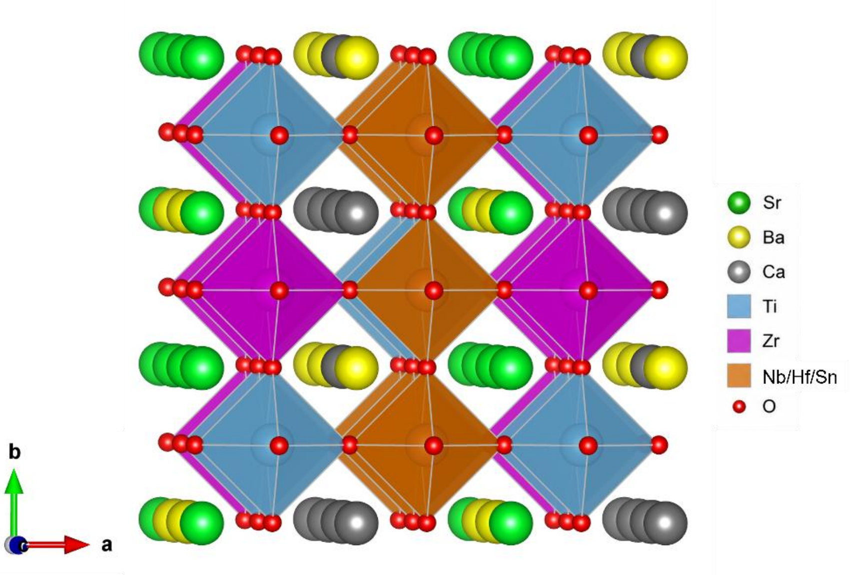

Figure 1. Crystal structure of $(Ba_{0.33}Ca_{0.33}Sr_{0.33})(Ti_{0.33}Zr_{0.33}M_{0.33})O_3$ (M = Nb, Sn, or Hf)

The three selected HEPOs, $(Ba_{0.33}Ca_{0.33}Sr_{0.33})(Ti_{0.33}Zr_{0.33}M_{0.33})O_3$ (M = Nb, Sn, or Hf) were modelled using the SQS approach to represent the random distribution of cations, as illustrated in Fig. 1. The generated supercells were fully relaxed using DFT until both the total energy and atomic forces satisfied the prescribed convergence criteria. Following structural optimisation, all compositions retained the perovskite crystal structure without any indications of structural instability, demonstrating that the multicomponent compositions can be accommodated within a stable ABO_3 lattice.

Table 1. Volume (V), tolerance factor (t), theoretical density (d), and formation energy of $(Ba_{0.33}Ca_{0.33}Sr_{0.33})(Ti_{0.33}Zr_{0.33}M_{0.33})O_3$ (M = Nb, Sn, or Hf).

HEPO-M	V (Å^3)	t	d (kg/m^3)	Formation energy (eV/atom)
HEPO-Nb	805.51	0.99	5.29	-3.21
HEPO-Sn	817.06	0.98	5.42	-3.64
HEPO-Hf	819.71	0.97	5.89	-3.23

The optimised structural parameters, including the supercell volume (*V*), Goldschmidt tolerance factor (*t*), theoretical density (*d*), and formation energy, are summarised in Table 1. The fully relaxed structures confirm the thermodynamic stability of all three HEPO compositions. The optimized supercell volume increased from 805.51 Å^3 for HEPO-Nb to 817.06 Å^3 and 819.71 Å^3 for HEPO-Sn and HEPO-Hf, respectively. This trend reflects the differences in ionic radii and bonding characteristics of the substituted B-site cations. A corresponding increase in the theoretical density was also observed, with HEPO-Hf exhibiting the highest density owing to the significantly larger atomic mass of Hf.

All three compositions exhibited negative formation energies, ranging from -3.21 to -3.64 eV/atom, indicating favourable thermodynamic stability. Among the investigated compounds, HEPO-Sn possesses the lowest formation energy, suggesting that it is energetically more favourable than the Nb- and Hf-containing counterparts. The combination of negative formation energies and high configurational entropy further supports the feasibility of experimentally synthesising these compositionally complex perovskite oxides.

To elucidate the influence of B-site substitution on the electronic structure relevant to TE performance, the total and atom-projected density of states (DOS) were calculated all three compositions (Fig. 2). In each case, the valence band was dominated by O-2p states, while the conduction band was primarily composed of B-site cation *d* states. A significant difference was observed among the three systems. HEPO-Nb exhibits metallic behaviour, whereas both HEPO-Sn and HEPO-Hf retain semiconducting characteristics. The metallic character of HEPO-Nb originates from the of Nb^{5+}, which acts as a donor by supplying additional electrons to the conduction band. In contrast, the atom-projected DOS revealed that Sn-derived states contribute less to the conduction band region than those of Nb and Hf, suggesting a weaker participation of Sn orbitals in the electronic states governing charge transport.

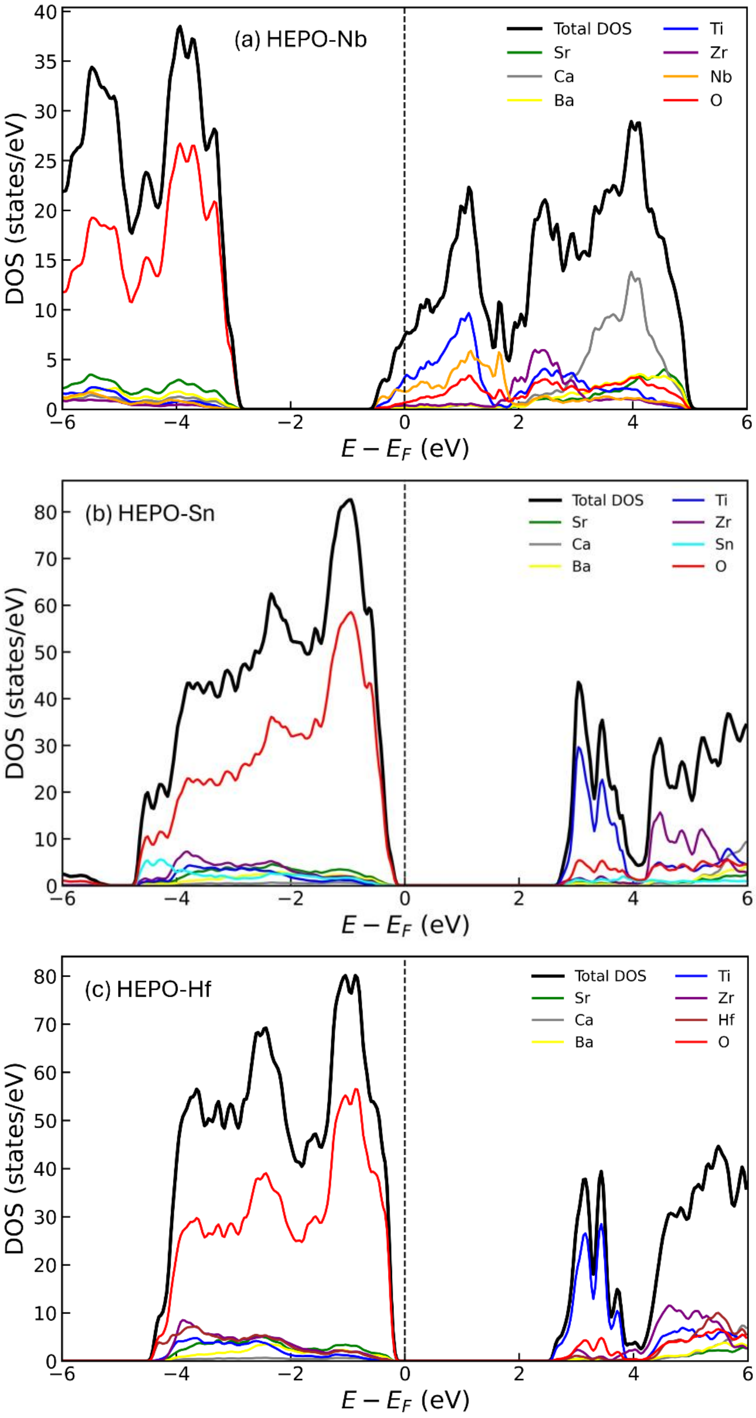

Figure 2. Total and partial density of states of (a) HEPO-Nb, (b) HEPO-Sn, (c) HEPO-Hf

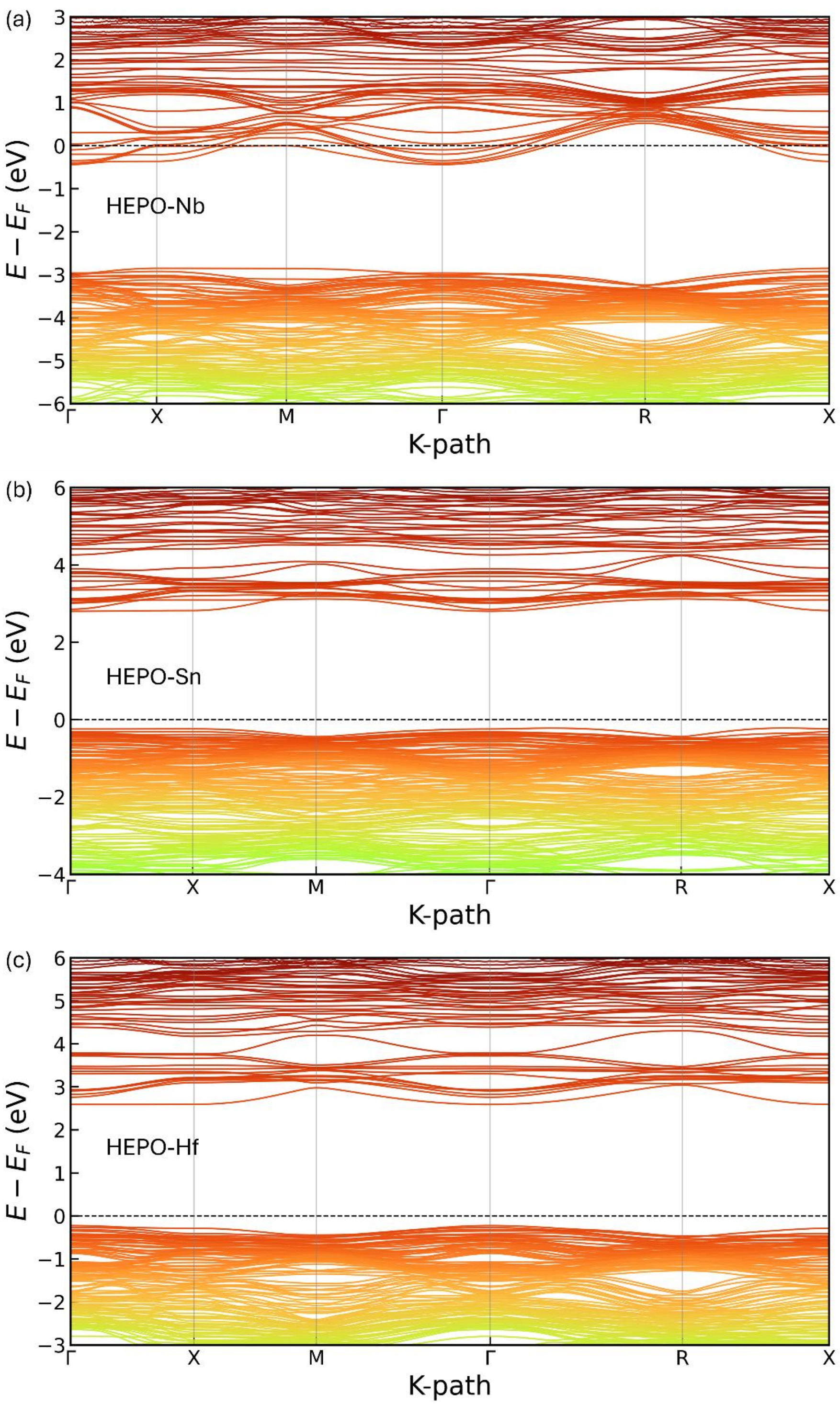

Figure 3. Electronic band structure of (a) HEPO-Nb, (b) HEPO-Sn, (c) HEPO-Hf

The electronic structures inferred from the DOS analysis are further confirmed by the calculated electronic band structures shown in Fig. 3. Consistent with the DOS results, HEPO-Nb exhibits metallic *n*-type behaviour, with the Fermi level crossing the conduction band. In contrast, HEPO-Sn and HEPO-Hf remain semiconducting, with calculated band gaps of 3.02 and 2.82 eV, respectively. The distinct electronic behaviour arises from the different valence states of the substituent cations. While Nb^{5+} introduces excess electrons that shift the Fermi level into the conduction band, the isovalent Sn^{4+} and Hf^{4+} primarily modify the electronic structure through orbital hybridisation without significantly altering the carrier concentration. Consequently, HEPO-Nb is expected to exhibit superior electrical conductivity, whereas the semiconducting HEPO-Sn and HEPO-Hf compositions are likely to possess higher Seebeck coefficients. These results demonstrate that B-site compositional engineering provides an effective strategy for tailoring the electronic structure and thermoelectric performance of high-entropy perovskite oxides.

2.3 Calculated electronic thermoelectric properties of $(Ba_{0.33}Ca_{0.33}Sr_{0.33})(Ti_{0.33}Zr_{0.33}M_{0.33})O_3$

The influence of Nb, Sn, and Hf substitution at the B-site on the electronic transport properties, namely the Seebeck coefficient (S), electrical conductivity (σ/τ), and electronic thermal conductivity (κ_e/τ), was investigated using the BoltzTraP2 code, which employs the semiclassical Boltzmann transport formalism within the constant relaxation time approximation. To comprehensively evaluate the electronic transport behaviour, all transport coefficients were calculated under both *n*-type and *p*-type doping conditions. However, owing to the metallic nature of HEPO-Nb predicted by the electronic structure calculations, only *n*-type transport properties were considered for this composition, whereas both *n*-type and *p*-type transport characteristics were evaluated for the semiconducting HEPO-Sn and HEPO-Hf compounds.

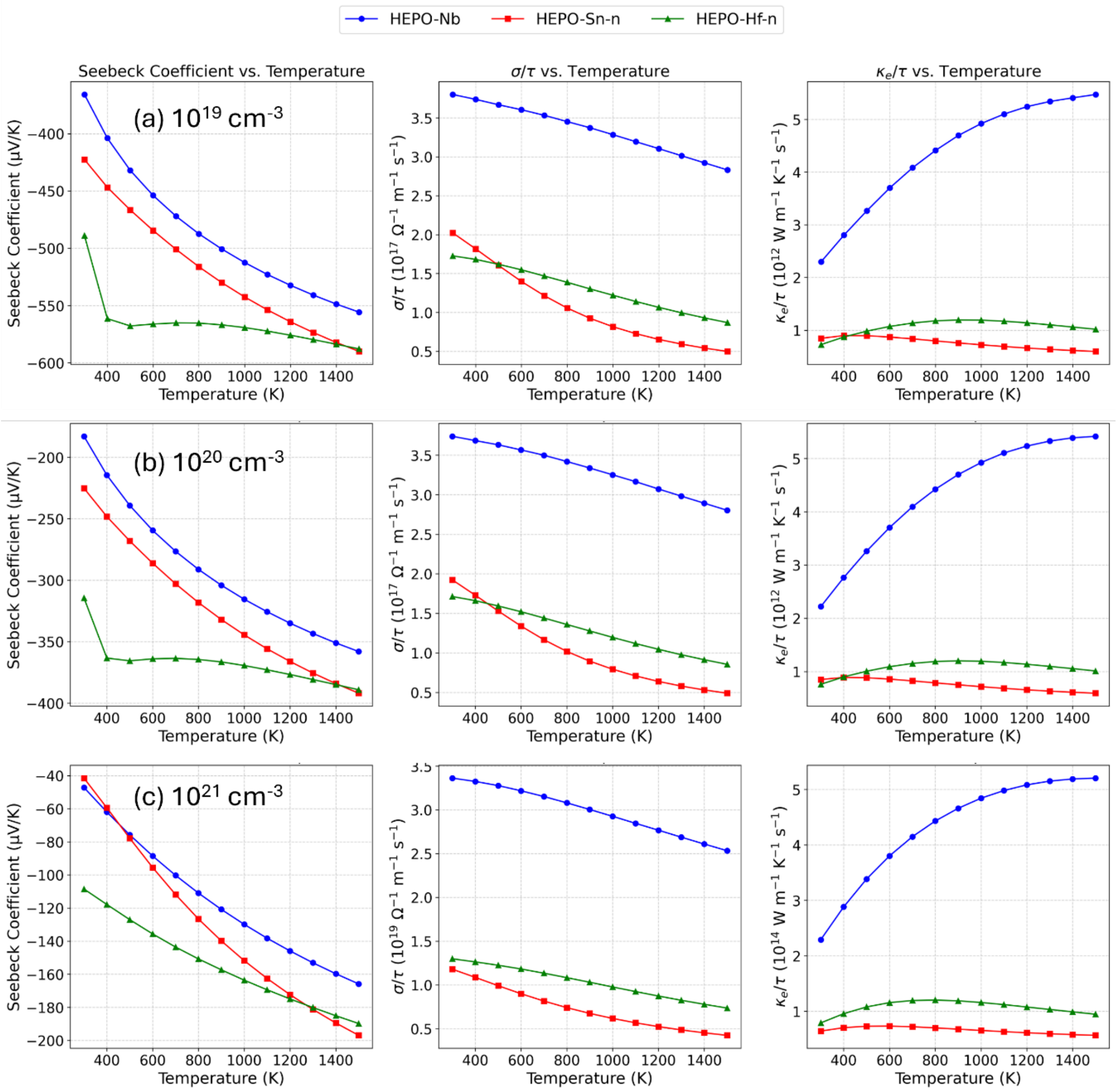

Figure 4. Temperature dependence of the Seebeck coefficient, electrical conductivity, and electronic thermal conductivity of HEPO-Nb, HEPO-Sn, and HEPO-Hf at (a) 10^{19} cm^{-3}, (b) 10^{20} cm^{-3}, and (c) 10^{21} cm^{-3} under n-type conduction.

2.3.1 n-type conduction

For n-type conduction, three carrier concentrations of 10^{19} cm^{-3}, 10^{20} cm^{-3}, and 10^{21} cm^{-3} were selected to evaluate the TE performance of the three HEPO compositions, as shown in Fig. 4 (a – c). Among the investigated compounds, HEPO-Hf composition exhibited the highest absolute Seebeck coefficient throughout the investigated temperature range, whereas HEPO-Nb showed the lowest values, particularly at higher carrier concentrations. This behaviour is consistent with the metallic character of HEPO-Nb, where electron donation by Nb^{5+} substantially increases the carrier concentration, thereby reducing the thermopower. This is also the reason why HEPO-Nb exhibited the highest electrical conductivity (σ/τ) across the entire temperature range for all investigated carrier concentrations, followed by HEPO-Hf and HEPO-Sn. The comparatively lower conductivity of HEPO-Sn is consistent with the weaker contribution of Sn-derived states to the conduction band, as revealed by the projected DOS. The electronic thermal conductivity (κ_e/τ) followed a similar trend to the electrical conductivity, with the metallic HEPO-Nb exhibiting substantially higher values than the semiconducting HEPO-Sn and HEPO-Hf compounds.

Overall, in the case of n-type doping, the HEPO-Nb composition offers superior electrical conductivity at the expense of a reduced Seebeck coefficient, whereas HEPO-Hf offers a more favourable balance between thermopower and electrical conductivity. The comparatively low conductivity of HEP-Sn limits its predicted *n*-type TE performance.

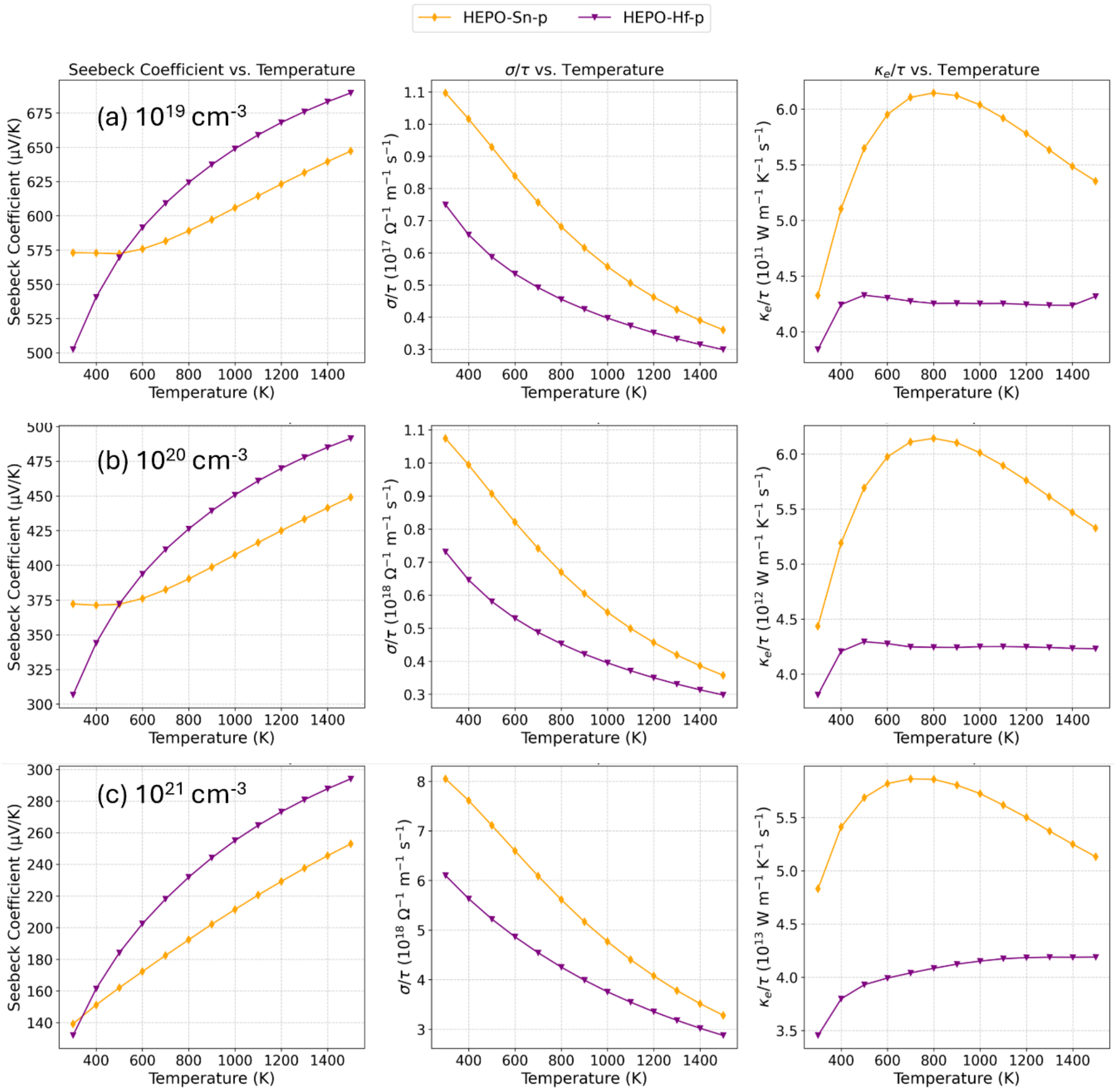

Figure 5. Temperature dependence of the Seebeck coefficient, electrical conductivity, and electronic thermal conductivity of HEPO-Sn and HEPO-Hf at (a) 10^{19} cm^{-3}, (b) 10^{20} cm^{-3}, and (c) 10^{21} cm^{-3} under p-type conduction.

2.3.2 p-type conduction

Since HEPO-Sn and HEPO-Hf exhibit semiconducting electronic structures with finite band gaps, their *p*-type transport properties were additionally evaluated at carrier concentrations of 10^{19} cm^{-3}, 10^{20} cm^{-3}, and 10^{21} cm$^{-3,}$ as shown in Fig. 5. A comparison between the two compositions revealed that HEPO-Hf consistently exhibits higher Seebeck coefficients than HEPO-Sn over the investigated temperature and carrier concentration ranges. In contrast to the *n*-type results, HEPO-Sn displays higher electrical conductivity (σ/τ) and electronic thermal conductivity (κ_e/τ) than HEPO-Hf. This behaviour reflects the different valence-band characteristics introduced by Sn and Hf substitution.

Overall, the calculated *p*-type transport properties revealed a clear trade-off between the two semiconducting compositions. HEPO-Hf offers larger Seebeck coefficients but lower electrical conductivity, whereas HEPO-Sn exhibits enhanced electrical conductivity at the expense of reduced thermopower. Consequently, the optimum *p*-type thermoelectric performance depends on achieving an appropriate balance between these competing transport parameters.

2.3.3 Power factor analysis

The calculated power factors for all investigated transport scenarios are presented in Fig. 6. Among all compositions, HEPO-Nb consistently exhibited the highest power factor under *n*-type conduction across the investigated carrier concentrations. This behaviour arises primarily from its metallic character and the high electrical conductivity resulting from Nb-induced electron donation, which compensates for its comparatively lower Seebeck coefficient.

For the semiconducting compositions, HEPO-Hf generally exhibits higher *n*-type power factors than HEPO-Sn owing to its more favourable balance between electrical conductivity and thermopower. Furthermore, both HEPO-Sn and HEPO-Hf display higher power factors under *n*-type conduction than under *p*-type conduction, particularly at low and intermediate carrier concentrations.

Overall, the calculated power factor trends are consistent with the electronic structure analysis, confirming that B-site compositional engineering effectively tunes the electronic transport properties of high-entropy perovskite oxides. These theoretical predictions served as the basis for the subsequent experimental synthesis, structural characterisation, and thermoelectric measurements presented in the following sections.

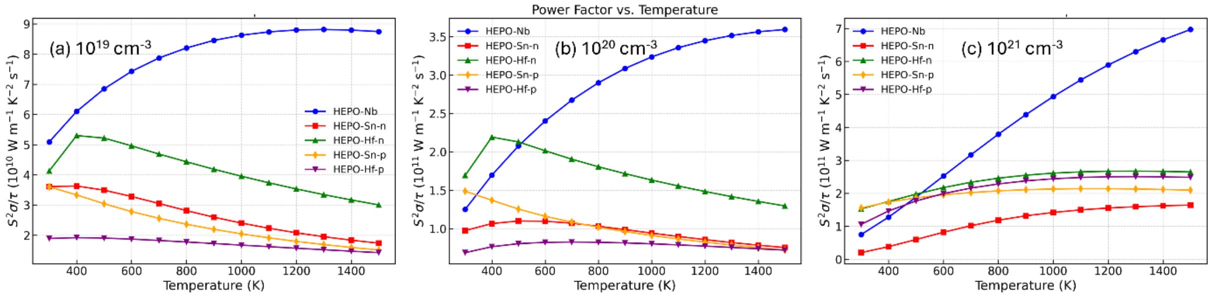

Figure 6. Temperature dependence of the calculated power factor for HEPO-Nb, HEPO-Sn, and HEPO-Hf at carrier concentrations of (a) 10^{19} cm^{-3}, (b) 10^{20} cm^{-3}, and (c) 10^{21} cm^{-3}.

3. Experimental validation of theoretical predictions

3.1. Experimental methods

The three selected compositions, HEPO-Nb, HEPO-Sn, and HEPO-Hf, were synthesised by a conventional solid-state route involving planetary ball milling followed by consolidation using spark plasma sintering (SPS). The starting materials were $BaCO_3$ (99%), $CaCO_3$ (99.95–100.05%), $SrCO_3$ (99%), and SnO_2 (99.9%) purchased from Sigma-Aldrich, together with TiO_2 (99.6%), HfO_2 (99%; metals basis excluding Zr, Zr < 1.5%), and Nb_2O_5 (99.9%) supplied by Thermo Fisher Scientific.

The precursor powders were weighed according to the required stoichiometric ratios and mixed with 100 mL of isopropyl alcohol (IPA) in a zirconia milling jar. Ball milling was carried out using a planetary ball mill (PM 100, Retsch) at 250 rpm for 2 h. Following milling, the slurry was vacuum evaporated to remove the IPA, and the resulting powder was dried in a hot-air oven overnight (12–18 h). The dried powders were calcined at 1100 °C for 4 h in air.

The calcined powders were consolidated using a spark plasma sintering system (DSP 507, Dr. Fritsch). Based on preliminary optimisation, the final sintering conditions were established as 1400°C under a uniaxial pressure of 50 MPa in a helium atmosphere, with a heating rate of 100°C min^{-1}. The calcination step was found to be essential for improving the relative density of the sintered ceramics and for removing residual volatile species remaining after powder processing.

The bulk densities of the sintered samples were determined using the Archimedes method. The relative density was calculated as $(\rho_{exp}/\rho_{th}) \times 100\%$, while the corresponding porosity was determined as $(1 - \rho_{exp}/\rho_{th}) \times 100\%$, where ρ_{exp} is the experimentally obtained density, and ρ_{th} is the theoretical density calculated from the XRD-derived lattice parameters. Phase identification was performed by powder X-ray diffraction (XRD) using a PANalytical X'Pert Pro diffractometer equipped with Cu Kα radiation. Diffraction patterns were collected over a 2θ range of 10–100°. The microstructure of polished samples (final polish using 0.1 μm colloidal silica) was examined by field-emission scanning electron microscopy (FE-SEM; FEI Quanta FEG 250) operated at an accelerating voltage of 10 kV. The elemental composition was analysed by energy-dispersive X-ray spectroscopy (EDS, Bruker) at an accelerating voltage of 20 kV.

The chemical states of the constituent elements were investigated by X-ray photoelectron spectroscopy (XPS) using a Thermo Scientific K-Alpha spectrometer. Charge correction for the XPS was done using the adventitious carbon C 1s peak at 284.8 eV as the reference. Peak fitting and deconvolution were carried out using Avantage software after Shirley/Lorentzian-Gaussian background subtraction. The high-resolution spectra of all elements underwent meticulous fitting and peak separation to achieve a precise and comprehensive characterization of the chemical bonding states and electronic structures of the analysed material.

The electrical conductivity and Seebeck coefficient were measured using a ProboStat™ measurement cell (NorECs AS) employing the in-plane Van der Pauw method in a cross-plane configuration under a flowing helium atmosphere. Measurements were performed between 200 and 1000 °C during both heating and cooling cycles at a rate of 200 °C h^{-1}, using a temperature interval of 100 °C with a dwell time of 3 h at each temperature.

The total thermal conductivity (κ) was calculated according to: $\kappa = \rho\alpha C_p$, where ρ is the bulk density, α is the thermal diffusivity, and Cp is the specific heat capacity, estimated using the rule of mixtures. Thermal diffusivity was determined using a laser flash analyser (Linseis LFA 1000, Germany) under a vacuum from room temperature up to 1000 °C at intervals of 100 °C. Measurements were performed on polished disc samples with a diameter of 15 mm.

3.2. Structural and microstructural characterisation

The X-ray diffraction (XRD) patterns of the synthesised HEPO-Nb, HEPO-Sn, and HEPO-Hf samples, together with the reference diffraction peaks of cubic $SrTiO_3$, are presented in Fig. 7. All three compositions predominantly crystallised in the cubic perovskite structure ($Pm\bar{3}m$). Minor secondary phases were detected in the HEPO-Sn sample, which may be attributed to an incomplete solid-state reaction, local compositional inhomogeneity, or the limited solubility of certain cations within the high-entropy perovskite lattice [18]. The diffraction peaks of the HEPO-Hf sample were noticeably broader than those of HEPO-Nb and HEPO-Sn, indicating a smaller crystallite size. The average crystallite size, estimated using the Scherrer equation, was approximately 11.8 nm for HEPO-Hf, compared with 20.8 nm and 25.7 nm for HEPO-Nb and HEPO-Sn, respectively.

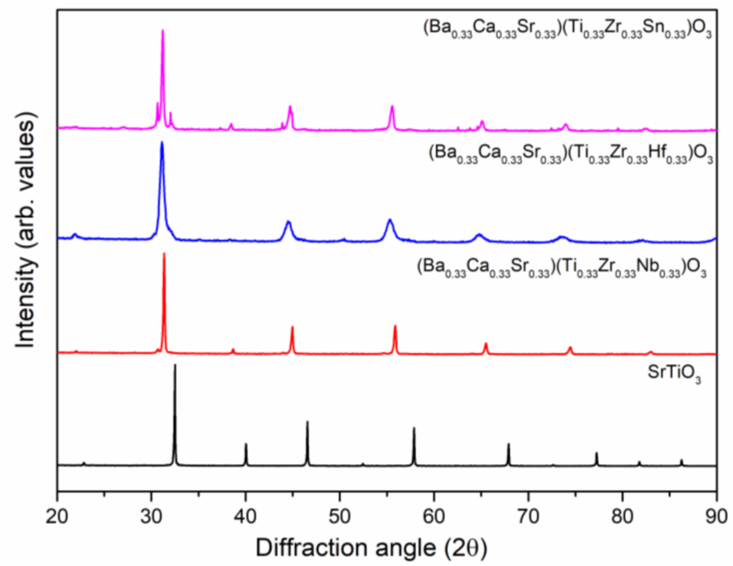

Figure 7. XRD patterns of HEPO-Nb, HEPO-Sn, and HEPO-Hf together with the reference diffraction peaks of cubic $SrTiO_3$.

The fracture surface morphologies of the sintered samples are shown in Fig. 8. The average grain size was determined considering at least 300 grains using ImageJ software. HEPO-Hf exhibited the finest microstructure, with an average grain size of approximately 0.2 ± 0.1 μm. HEPO-Sn showed intermediate grain growth, with an average grain size of approximately 0.4 ± 0.1 μm, whereas HEPO-Nb exhibited significantly larger grains, averaging approximately 5.0 ± 0.3 μm. The observed grain-size trend is consistent with the crystallite-size analysis obtained from XRD. Energy-dispersive X-ray spectroscopy (EDS) elemental mapping (not shown here) confirmed a homogeneous distribution of all constituent elements (Ba, Ca, Sr, Ti, Zr, Nb/Sn/Hf, and O) throughout the microstructure, indicating good compositional uniformity of the synthesised high-entropy perovskite oxides.

HEPO-Nb exhibited the highest degree of densification, with a relative density of 96.6% and a corresponding porosity of 3.4%. HEPO-Sn achieved a relative density of 94.0% (6.0% porosity), whereas HEPO-Hf exhibited the lowest relative density of 91.9%, corresponding to a porosity of 8.1%.

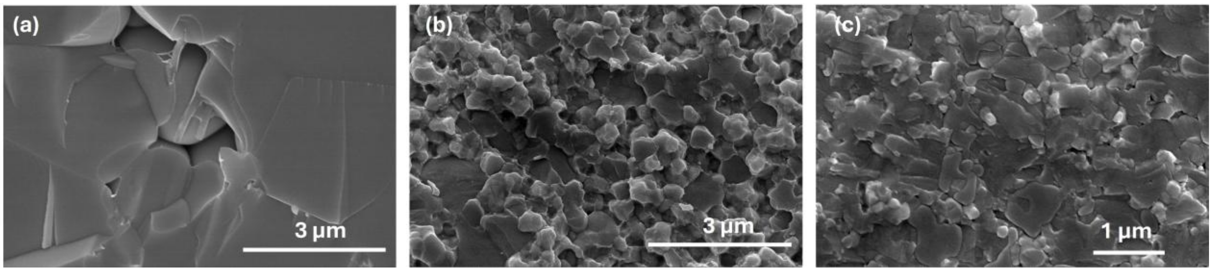

Figure 8. SEM micrographs of fractured surface: a) HEPO-Nb, b) HEPO-Sn, and c) HEPO-Hf.

X-ray photoelectron spectroscopy (XPS) was employed to investigate the surface chemical states of the constituent elements and to evaluate the concentration of oxygen vacancies in the synthesised high-entropy perovskite oxides. No additional chemical species attributable to impurity phases were detected within the detection limit of the XPS measurements, indicating the successful synthesis of the targeted compositions. The XPS spectra confirmed that the A-site cations Ba, Ca, and Sr are predominantly present in the +2 oxidation state, while Zr exists exclusively as Zr^{4+} in all three compositions.

The O1s spectra of HEPO-Nb, HEPO-Hf, and HEPO-Sn are presented in Fig. 9(a), 10(a), and 11(a), respectively. For HEPO-Nb and HEPO-Hf, the spectra were deconvoluted into three components corresponding to lattice oxygen (O_{Lat}), oxygen-vacancy-related species (O_{Vac}), and surface-adsorbed oxygen (O_{Ads}). For HEPO-Nb, these peaks were centred at 529.56, 531.03, and

532.23 eV, respectively [19]. Similarly, the O 1s spectrum of HEPO-Hf exhibited lattice oxygen, oxygen-vacancy, and adsorbed oxygen peaks at 529.62, 531.17, and 532.86 eV, respectively [20]. In contrast, the O1s spectrum of HEPO-Sn required four components for an adequate fit. Two lattice oxygen peaks located at 528.73 and 529.13 eV indicate local lattice distortions arising from the highly disordered distribution of A- and B-site cations. The oxygen-vacancy-related component (O_{Vac}) was identified at 530.76 eV, while the high-binding-energy peak at 531.47 eV was assigned to surface hydroxyl groups and adsorbed carbonate or molecular water species [19].

The corresponding C1s spectra, shown in Fig. 9(b), 10(b), and 11(b), exhibited the characteristic adventitious carbon peak at approximately 284.8 eV (which was used as the charge correction reference) together with C–O and O–C=O components originating from surface hydroxyl and carbonate species formed due to adsorption of atmospheric CO_2 on the oxide surface. In addition, a weak satellite carbon peak at 292.64 eV was observed for the HEPO-Hf composition [21].

The total oxygen vacancies were calculated by taking into account the C1s C-O-C and O-C=O peaks [22]. Quantitative analysis showed the oxygen-vacancy concentrations of approximately 2.48%, 6.13%, and 7.96 % for HEPO-Nb, HEPO-Hf, and HEPO-Sn, respectively. The comparatively higher oxygen-vacancy concentration observed in HEPO-Sn suggests that Sn substitution promotes defect formation within the perovskite lattice. The coexistence of multiple transition-metal cations is expected to facilitate charge-compensation mechanisms involving changes in cation oxidation state, thereby promoting oxygen-vacancy formation. Furthermore, the reducing argon atmosphere employed during SPS sintering is likely to favour oxygen loss during densification, contributing to the relatively high oxygen-vacancy concentrations observed in these non-annealed ceramics [23].

The transition-metal core-level spectra further support the proposed defect chemistry. The Nb3d spectrum (Fig. 9(c)) reveals the coexistence of Nb^{5+} and Nb^{4+} species, with Nb^{5+} peaks located at 209.21 and 206.48 eV and Nb^{4+} peaks at 207.62 and 205.23 eV, indicating partial reduction of Nb during processing [24]. Similarly, the Hf4f spectrum (Fig. 10(c)) is dominated by Hf^{4+}, with $Hf4f_{7/2}$ and $Hf4f_{5/2}$ peaks appearing at 16.26 and 17.94 eV, respectively. Minor metallic Hf^0 peaks were also detected at 13.73 and 15.50 eV, together with a characteristic HfO_2 loss feature at 24.59 eV [25].

The Sn3d spectrum of HEPO-Sn (Fig. 11(c)) is dominated by Sn^{4+}, with characteristic $Sn3d_{5/2}$ and $Sn3d_{3/2}$ peaks located at 485.72 and 494.12 eV, respectively. A minor Sn^{2+} contribution was also identified at 483.57 and 491.97 eV, accounting for only approximately 0.44% of the total Sn signal [26]. The presence of this small fraction of reduced Sn species indicates local charge compensation associated with oxygen-vacancy formation while confirming that tin remains predominantly stabilised in the tetravalent oxidation state.

The Ti2p spectra, shown in Fig. 9(d), 10(d), and 11(d), revealed distinct differences among the three compositions. Both HEPO-Nb and HEPO-Hf exhibit mixed Ti^{3+}/Ti^{4+} valence states, whereas only Ti^{4+} is detected in HEPO-Sn. Specifically, Ti^{4+} peaks were observed at 457.91/463.91 eV for HEPO-Nb and 457.99/463.72 eV for HEPO-Hf, while Ti^{3+} components appeared at 457.03/463.03 eV and 456.37/462.37 eV, respectively. In contrast, the Ti2p spectrum of HEPO-Sn exhibited only Ti^{4+} peaks located at 457.60 and 463.25 eV, indicating the absence of detectable Ti reduction [23].

Overall, the XPS analysis confirmed the successful incorporation of multiple cation species into the high-entropy perovskite lattice and revealed the presence of mixed-valence cations together with significant oxygen-vacancy concentrations. The coexistence of Ti^{3+}/Ti^{4+}, Nb^{4+}/Nb^{5+}, and Sn^{2+}/Sn^{4+} oxidation states indicates that charge compensation occurs through both cation reduction and oxygen-vacancy formation. These defect features are expected to strongly influence the thermoelectric behaviour of the investigated materials. Oxygen vacancies can increase the carrier concentration and modify the electronic band structure, while the severe lattice distortion associated with the high-entropy configuration enhances phonon scattering, thereby reducing the lattice contribution to the thermal conductivity. Consequently, the observed defect chemistry provides an important mechanism for tailoring the electrical and thermal transport properties of high-entropy perovskite oxides.

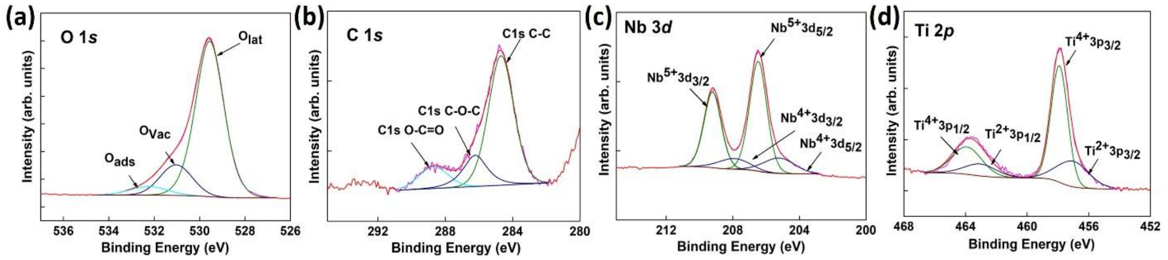

Figure 9. High-resolution XPS spectra of HEPO-Nb showing the (a) O 1s, (b) C 1s, (c) Nb 3d, and (d) Ti 2p core-level spectra

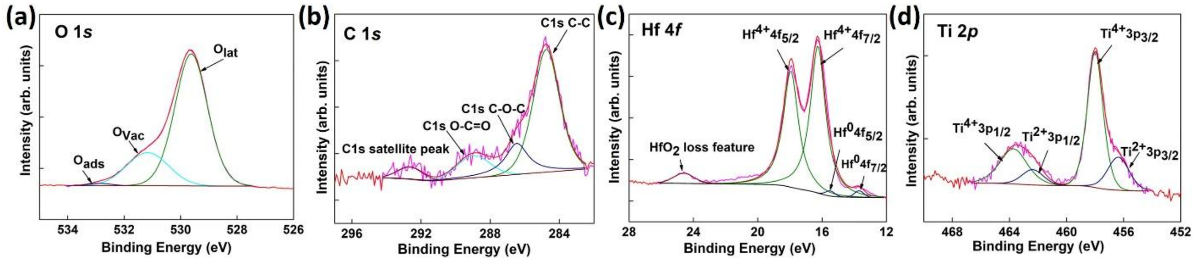

Figure 10. High-resolution XPS spectra of HEPO-Hf showing the (a) O 1s, (b) C 1s, (c) Hf 4f, and (d) Ti 2p core-level spectra

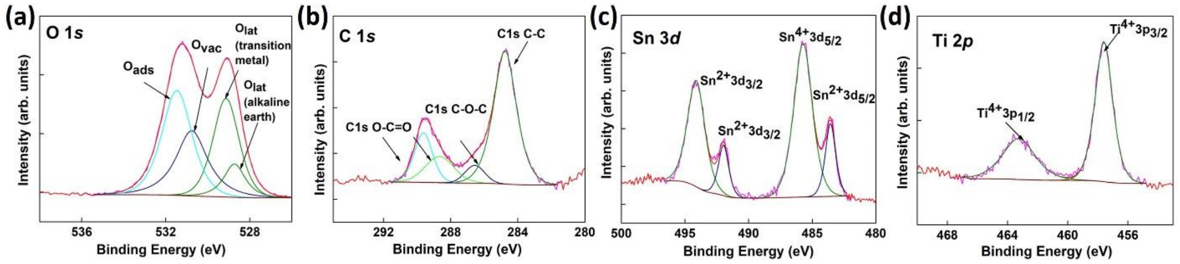

Figure 11. High-resolution XPS spectra of HEPO-Sn showing the (a) O 1s, (b) C 1s, (c) Sn 3d, and (d) Ti 2p core-level spectra

3.3 Measurement of thermoelectric properties

The experimentally measured thermoelectric properties of the synthesised HEPO ceramics are presented in Fig. 12. The temperature dependence of the thermal conductivity is shown in Fig. 12(a). Among the investigated compositions, HEPO-Hf exhibited the lowest thermal conductivity over the entire temperature range, decreasing from approximately 1.80 $Wm^{-1}K^{-1}$ at room temperature to 1.68 $Wm^{-1}K^{-1}$ at 1000 °C. This reduced thermal conductivity is primarily attributed to its fine-grained microstructure and high concentration of lattice defects, including oxygen vacancies, which enhance phonon scattering and suppress lattice heat transport [27]. In comparison, HEPO-Nb exhibited intermediate thermal conductivity values, decreasing from approximately 2.60 to 2.20 $Wm^{-1}K^{-1}$, whereas HEPO-Sn showed values ranging from approximately 2.10 to 1.87 $Wm^{-1}K^{-1}$ over the same temperature range.

The temperature dependence of the Seebeck coefficient is presented in Fig. 12(b). The experimental measurements are generally consistent with the theoretical predictions obtained from the electronic structure calculations. HEPO-Nb exhibited a negative Seebeck coefficient throughout the investigated temperature range, confirming dominant *n*-type charge transport arising from Nb-induced electron donation. The calculations further suggested that the semiconducting HEPO-Hf and HEPO-Sn compositions could exhibit either *n*-type or *p*-type conduction depending on the defect chemistry and carrier concentration. Experimentally, HEPO-Hf also displayed a negative Seebeck coefficient, whereas HEPO-Sn exhibited a positive Seebeck coefficient over the measured temperature range, indicating dominant *n*-type and *p*-type conduction, respectively. These results demonstrate that subtle differences in defect chemistry and carrier concentration strongly influence the transport behaviour of the semiconducting high-entropy perovskite oxides.

The electrical conductivity measurements revealed that reliable data could not be obtained for HEPO-Sn above approximately 500°C and for HEPO-Hf above approximately 700°C because the electrical resistance exceeded the measurement limit of the experimental setup. The relatively high porosity of HEPO-Sn (6.0%) and HEPO-Hf (8.1%), together with their fine-grained microstructures, is expected to increase carrier scattering and reduce electrical conductivity, resulting in extremely high electrical resistance at elevated temperatures [28]. Furthermore, the comparatively weak contribution of Sn-derived electronic states to the conduction band, as predicted by the density-of-states calculations, provides an additional explanation for the poor electrical conductivity of HEPO-Sn.

The temperature dependence of the dimensionless thermoelectric figure of merit (*ZT*) is presented in Fig. 12(c). Among the investigated compositions, HEPO-Hf achieved the highest *ZT* values throughout the measured temperature range, followed by HEPO-Nb. Although HEPO-Nb exhibited the highest electrical conductivity, its thermoelectric performance was limited by the relatively low Seebeck coefficient associated with its metallic character. In contrast, HEPO-Hf benefited from a more favourable balance between electrical and thermal transport properties, combining comparatively low thermal conductivity with a higher Seebeck coefficient. Overall, the experimental results are in good agreement with the theoretical predictions and demonstrate that B-site compositional engineering provides an effective strategy for optimising the thermoelectric performance of high-entropy perovskite oxides.

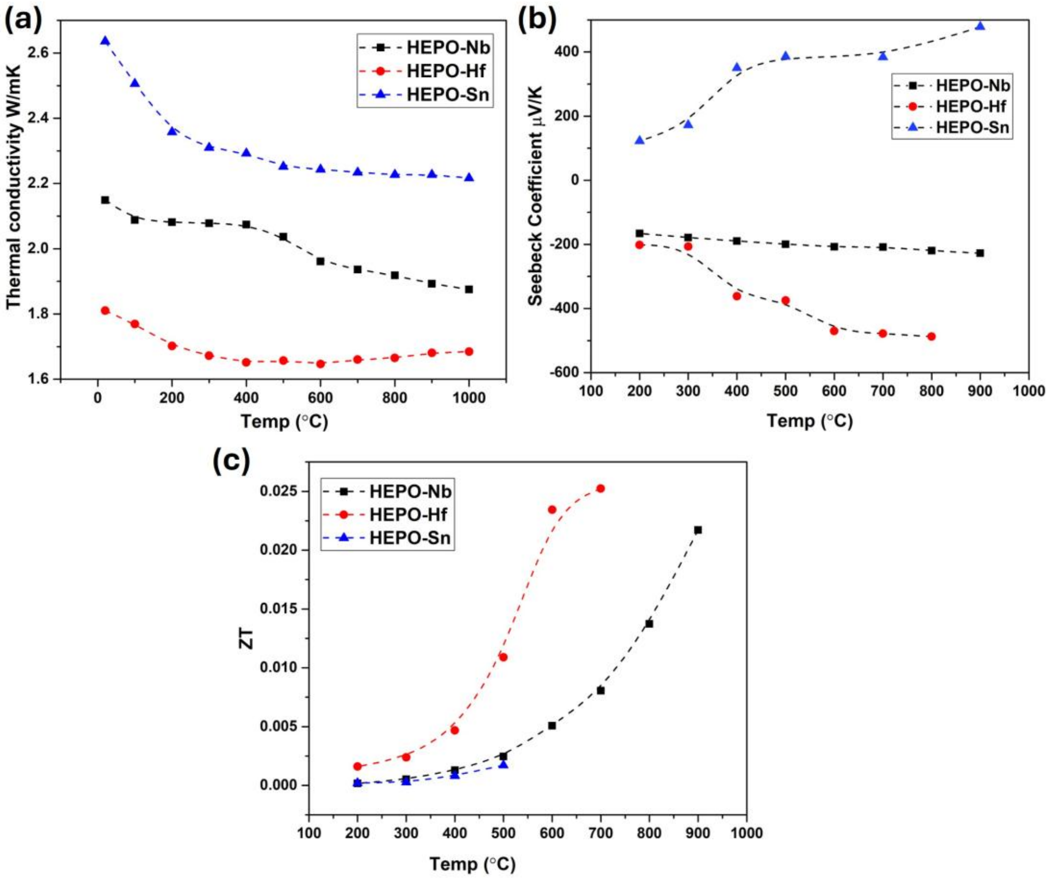

Figure 12. Temperature dependence of the (a) thermal conductivity, (b) Seebeck coefficient, and (c) dimensionless thermoelectric figure of merit (ZT) of the HEPO-Nb, HEPO-Sn, and HEPO-Hf compositions.

4. Conclusion

In this work, the structural, electronic, and thermoelectric properties of the high-entropy perovskite oxides $(Ba_{0.33}Ca_{0.33}Sr_{0.33})(Ti_{0.33}Zr_{0.33}M_{0.33})O_3$ (M = Nb, Sn, and Hf) were systematically investigated by combining first-principles density functional theory calculations with comprehensive experimental characterisation. The computational results demonstrated that B-site substitution strongly influences the electronic structure and transport behaviour of the investigated compounds. Specifically, Nb incorporation induced metallic behaviour through electron donation, resulting in enhanced electrical conductivity and power factor, whereas the Sn- and Hf-containing compositions retained semiconducting characteristics. Furthermore, the relatively weak contribution of Sn-derived electronic states near the Fermi level accounted for the comparatively low electrical conductivity predicted for HEPO-Sn.

The experimental results were in good agreement with the theoretical predictions and confirmed that B-site compositional engineering is an effective strategy for tailoring the thermoelectric performance of high-entropy perovskite oxides. Although HEPO-Nb exhibited superior electrical transport properties, HEPO-Hf achieved the highest thermoelectric figure of merit owing to its significantly reduced thermal conductivity, arising from enhanced phonon scattering associated with its fine-grained microstructure and defect-rich lattice. These results demonstrated that optimising the balance between electrical transport and thermal conductivity is essential for achieving high thermoelectric performance.

Overall, this work established a clear structure–property relationship linking B-site chemistry, electronic structure, defect chemistry, and thermoelectric performance in high-entropy perovskite oxides. The combined theoretical and experimental approach provides valuable design guidelines for the development of next-generation oxide thermoelectric materials and identifies HEPO-Hf as a promising candidate for high-temperature thermoelectric energy harvesting. Further improvements in thermoelectric performance are expected through optimisation of carrier concentration, defect chemistry, and microstructural engineering.

Acknowledgement

Funded by the EU NextGeneration EU through the Recovery and Resilience Plan for Slovakia under the project No. 09I03-03-V03-00094/2024/VA.

References

[1] Wu, Y., Chen, Z., *et al.*, Lattice Strain Advances Thermoelectrics, *Joule, 3* (2019), 5, pp.1276-1288 10.1016/j.joule.2019.02.008

[2] Hochbaum, A. I. , Chen, R., *et al*., Enhanced thermoelectric performance of rough silicon nanowires, *Nature, 451* (2008), 7175, 163-167 10.1038/nature06381

[3] Kim, S.I., Lee, K.,H., *et al*., Dense dislocation arrays embedded in grain boundaries for high-performance bulk thermoelectrics, *Science, 348* (2015) pp. 109-114 10.1126/science.aaa4166

[4] Tritt, T. M., Holey and Unholey Semiconductors, *Science, 283* (1999), pp 804- 805 10.1126/science.283.5403.804.

[5] DiSalvo, F. J., Thermoelectric cooling and power generation, *Science, 285* (1999), pp. 703-706 10.1126/science.285.5428.703

[6] Wang, Y., Robson, M. J., *et al.*, High-entropy perovskites materials for next-generation energy applications, *Joule, 7* (2023), 5, pp. 843-854 10.1016/j.joule.2023.03.020

[7] Konstantinova, E. I., Litvinov, V. A., *et al*., Electron transport and thermoelectric properties in (Pb,Ho)-modified $Ca_{0.5}Sr_{0.5}MnO_{3-\delta}$ manganites with perovskite-type structure, *Ceram. Int., 50* (2024), 7, pp. 10144-10151 10.1016/j.ceramint.2023.12.324

[8] Yan, X., Poudel, B., *et al*., Experimental studies on anisotropic thermoelectric properties and structures of n-type $Bi_2Te_{2.7}Se_{0.3}$, *Energy Environ. Sci., 5* (2012), pp. 3373-3378 10.1021/nl101156v

[9] Mizoguchi, H., Eng, *et al.*, Probing the electronic structures of ternary perovskite and pyrochlore oxides containing Sn^{4+} or Sb^{5+}, *Inorg. Chem., 43* (2004), pp. 1667-1680 10.1021/ic034551c

[10] Hafner, J., Ab-initio simulations of materials using VASP: Density-functional theory and beyond, *J. Comput. Chem*., *29* (2008), 13, pp. 2044-2078 10.1002/jcc.21057

[11] Kresse, G., Furthmüller, J., Efficient iterative schemes for ab initio total-energy calculations using a plane-wave basis set, *Phys. Rev. B, 54* (1996), 16, pp. 11169-11186 10.1103/PhysRevB.54.11169

[12] Blöchl, P. E., Projector augmented-wave method, *Phys. Rev. B, 50* (1994), 24, pp. 17953-17979 10.1103/PhysRevB.50.17953

[13] Perdew, J. P., Burke, K., *et al*., Generalized gradient approximation made simple, *Phys. Rev. Lett., 77* (1996), 18, pp. 3865-3868 10.1103/PhysRevLett.77.3865

[14] Perdew, J. P., Burke, K., *et al*., Erratum: Generalized gradient approximation made simple, *Phys. Rev. Lett*., *78* (1997), 7, pp. 1396-1396 10.1103/PhysRevLett.78.1396

[15] Zunger, A., Wei, S.H., *et al.*, Special quasirandom structures, *Phys. Rev. Lett., 65* (1990), 3, pp. 353-356, 10.1103/PhysRevLett.65.353

[16] van de Walle, A., Asta, M., *et al.*, The alloy theoretic automated toolkit: a user guide, *Calphad, 26* (2002),4, pp. 539-553, 10.1016/S0364-5916(02)80006-2

[17] Madsen, G. K. H., Carrete, J., *et al.*, BoltzTraP2, a program for interpolating band structures and calculating semi-classical transport coefficients, *Comput. Phys. Commun., 231* (2018), pp. 140-145 10.1016/j.cpc.2018.05.010

[18] Khandelwal, A., Singh, S., *et al.*, Synthesis-driven functionality in high-entropy materials, *Small, 21* (2025), 44, e2501703 10.1002/smll.202501703

[19] Wang, X., Zhang, Y., *et al*., CoFeNiMnZnB as a high-entropy metal boride to boost the oxygen evolution reaction., *ACS Appl. Mater. Interfaces, 14* (2022), 42, pp. 48212-48219 10.1021/acsami.2c13854

[20] Frankcombe, T. J., Liu, Y., Interpretation of oxygen 1s x-ray photoelectron spectroscopy of ZnO, *Chem. Mater.*, *35* (2023), 14, pp. 5468-5474 10.1021/acs.chemmater.3c00801

[21] Chiang, C. L., Yang, J. M., *Novel Fire Retardant Polymers and Composite Materials*, Woodhead Publishing, Sawston, UK, 2017

[22] Chen, C., Takumu, *et al*., Visible light-driven H_2O_2 photoelectrocatalytic synthesis over a tandem electrode strategy, *Photocatal. Res. Potential, 1* (2024), 2, 10003 10.35534/prp.2024.10003

[23] Wei, Z., Lou, Z., *et al*., Improving thermoelectric properties of high-entropy $(Ca_{0.27}Sr_{0.27}Ba_{0.27}La_{0.19})TiO_{3-\delta}$ ceramics through defect engineering by controlling the oxygen vacancy content, *Ceram. Int., 51* (2025), 4, pp. 4300-4309 10.1016/j.ceramint.2024.11.406

[24] Pelatti, S., Benedetti, S., *et al*., Niobium oxide films with variable stoichiometry: structure, morphology, and ultrafast dynamics, *J. Phys. Chem. C*, *129* (2025), 17, pp. 8206-8214 10.1021/acs.jpcc.4c08535
[25] Yang, C.-M., Wei, C.-H., *et al*., Flexible and disposable hafnium nitride extended gates fabricated by low-temperature high-power impulse magnetron sputtering, *Nanomaterials*, *14* (2024), 14, 1191 10.3390/nano14141191
[26] Mohamed, A. Y., Lee, S. J., *et al*., X-ray spectroscopy study on the electronic structure of Sn-added p-type SnO films, *J. Phys.: Condens. Matter*, *32* (2020), 6, 065503 10.1088/1361-648X/ab4f51
[27] Zheng, Y., Zou, M., *et al*., Electrical and thermal transport behaviours of high-entropy perovskite thermoelectric oxides, *J. Adv. Ceram.*, *10* (2021), 2, pp. 377-384 10.1007/s40145-021-0462-5
[28] Ghosh, D., Kumar, M. M., *et al*., Bifunctional catalytic activity of solvothermally synthesized CeO_2 nanosphere/NiO nanoflake nanocomposites, *ACS Appl. Energy Mater.*, *5* (2022), 5, pp. 5666-5679 10.1021/acsaem.1c04036